Volume 1 | Number 1 | Jan 2013 | Pages 1–100

Journal of
**Materials Chemistry A**

Materials for energy and sustainability
www.rsc.org/materialsA

Li⁺

ROYAL SOCIETY
OF CHEMISTRY

ROYAL SOCIETY
OF CHEMISTRY

www.rsc.org/materialsA

Journal Name

**ARTICLE TYPE**

# Synthesis of hydrogenated TiO$_2$/reduced-graphene oxide nanocomposite and their application in high rate lithium ion batteries

**Jie Wang, Laifa Shen, Ping Nie, Guiyin Xu, Bing Ding, Shan Fang, Hui Dou and Xiaogang Zhang\***

**Abstract**: Hydrogenated TiO$_2$/reduced-graphene oxide (H-TiO$_2$/RGO) nanocomposite is synthesised *via* a facile one-pot hydrogenation treatment process. The morphologies and structures are characterized by transmission electron microscopy (TEM) and X-ray diffraction (XRD). The nitrogen adsorption-desorption isotherms revealed that the H-TiO$_2$/RGO exhibited large specific surface area of 114.4 m$^2$ g$^{-1}$.
10 Compared with the TiO$_2$/RGO nanocomposite, the H-TiO$_2$/RGO nanocomposite exhibits much higher rate capability and better capacity retention. At a current rate of 5 C, the reversible capacity of the H-TiO$_2$/RGO electrode is up to 166.3 mAh g$^{-1}$ and with only 2.4% capacity loss after 100 cycles. The excellent electrochemical performance is highly relative to the high electronic conductivity derived from hydrogenated TiO$_2$ frameworks and the well-contact between zero-dimensional (0D) H-TiO$_2$ nanoparticle
15 with two-dimensional (2D) reduced-graphene oxide nanosheets, which efficiently shortened the Li$^+$ diffusion path lengths, enhanced electrolyte-active material contact area and facilitated rapid e$^-$ transfer.

## Introduction

Lithium ion batteries (LIBs) play a critical role in the wireless revolution of the last decade, and are poised to contribute to a
20 society that is less reliant on fossil fuels.[1-5] Graphite has been widely used as anode materials for commercial LIBs, which shows poor cycle life and low rate performance. Moreover, it may cause combustion or explosion at elevated temperatures during the high rate charging/discharging process.[6, 7] Therefore,
25 to meet the increasing demand for batteries with higher energy densities, it is essential to develop new electrodes made from durable, nontoxic, and inexpensive materials with high charge/discharge rate and higher reversible capacity.

Recently, extensive attention has been paid to the use of
30 nanostructured TiO$_2$ as the negative electrode material for LIBs.[8-12] Titania is becoming attractive as an anode material for lithium storage since it exhibits a relatively high lithium insertion/extraction voltage at about 1.7 V.[13, 14] This feature can efficiently avoid the formation of solid electrolyte interfacelayers
35 (SEI) and electroplating of lithium during the cycling processes.

Moreover, titania is an abundant, low cost and environmentally benign material with a very low volume change (3-4%),[15, 16] which is vital for large-scale energy storage. Unfortunately, the low lithium ion diffusion (~10$^{-15}$ cm$^2$ s$^{-1}$) and poor electronic
40 conductivity (~10$^{-13}$ S cm$^{-1}$) of titania constitute the two major obstacles for its practical application in lithium storage.[17] Given that a high overpotential is commonly applied during the cycling processes, thus its rate performances were dramatically decreased. [14, 15]

45 To circumvent the above drawback of titania, considerable efforts have been devoted to improving lithium ion diffusion kinetics and electronic conductivity of TiO$_2$. One of the efficient ways is to tailor the size and morphology of TiO$_2$, which mainly improves lithium ion diffusion kinetics. Nanostructured TiO$_2$,
50 such as nanotubes, nanofibers, nanosheets, nanowires, and nanoparticles have been reported extensively because of their short lithium diffusion length.[18-22] Another approach is to improve electronic conductivity of TiO$_2$ electrode by mixing them with carbonaceous materials (*e.g.* carbon nanotubes and
55 graphene).[23-26] Compared with other additives, graphene appears

particularly promising to improve the rate capability and cycle performance of titania owing to its unique characteristics including superior electrical conductivity, large surface area and excellent mechanical flexibility.[27, 28] In addition, the very serious agglomeration of the $TiO_2$ nanoparticals can effectively overcomed by uniformly anchoring the nanoparticals onto the surface of graphene sheets.

Despite $TiO_2$-based composites showed an better electrochemical performance, the intrinsic low electronic conductivity of $TiO_2$ does not change with incorporation of conducting materials. Recently, the introduction of $Ti^{3+}$ has been proved to be one of the most promising way to enhance its electronic conductivity by creating $Ti^{3+}$ sites of $TiO_2$ *via* hydrogenation.[29-34] Samuelis [35] *et al*. reported that the well balanced $Li^+/e^-$ transport in hydrogenated $TiO_2$ is a key factor for high electrochemical performance.

Herein, we report a renovated approach for the synthesis of hydrogenated $TiO_2$/reduced-graphene oxide nanosheets (H-$TiO_2$/RGO) through hydrogenation of $TiO_2$/graphite oxide ($TiO_2$/GO) nanocomposites under ambient pressure (Scheme 1). It is shoud be noted that the introduction of $Ti^{3+}$ sites into $TiO_2$ nanoparticals accompanied with the reduction of graphite oxide simultaneously. The facile hydrogenation process can confer upon $TiO_2$ high electronic conductivity. Due to the high electronic conductivity derived from hydrogenated $TiO_2$ frameworks and the well-contact between zero-dimensional (0D) H-$TiO_2$ nanoparticle with two-dimensional (2D) reduced-graphene oxide nanosheets, the three-dimensional (3D) H-$TiO_2$/RGO electrode exhibited excellent electrochemical performances such as high specific capacity, rate capability, and stable cycle life compared with those of the $TiO_2$/RGO and pure H-$TiO_2$ nanoparticals.
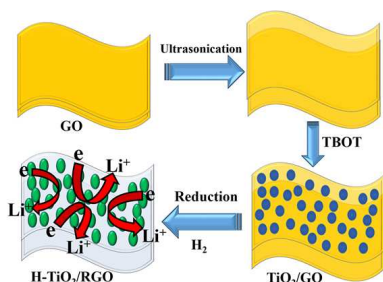


Scheme 1 Schemmatic illustration of the synthesis of H-$TiO_2$/RGO nanocomposite.

## Experimental

### Preparation of mesoporous H-$TiO_2$/RGO

All the reagents used for experiments were of analytical grade and used directly without further purification. Deionized water was used in all the processes involving aqueous solution preparation and washing. Graphene oxide (GO) was systhesized form graphite powder based on the modified Hummer's method as described elsewhere.[35] Typically, 90 mg GO was dispersed in 100 mL ethanol (EtOH) with the aid of ultrasonication for 4 h. Then 2.3 mL tetrabutyl titanate was added drop-by-drop into the suspension and the mixture was magnetically stirred for 30 min followed by the addition of 2.3 mL $H_2O$. Following the mixture was refluxed at 90 °C for 8 h. After the reaction, the suspension and precipitate were separated by centrifugation, washed with deionized water and ethanol and dried at 60 °C for 12 h. Subsequently, the powder was calcinated at 450 °C for 4 h under a flowing atmosphere of 5% $H_2$/95% $Ar_2$ to obtain the H-$TiO_2$/RGO nanocomposite. For comparsion, The process for preparing $TiO_2$-RGO mixture was similar to that of H-$TiO_2$/RGO preparation, except with the hydrazine hydrate (85%) as reductant was added and the prepared powder was calcinated at 450 °C for 4 h in a nitrogen atmosphere.

### Material characterization

The microstructural properties of the resultant nanocomposites were obtained using transmission electron microscopy (TEM, FEI, Tecnai-20) and high-resolution transmission electron microscopy (HRTEM, JEOL, JEM-2010). The crystal structure was characterized by X-ray diffraction (XRD) (Bruker D8 advance) with Cu Kα radiation. Thermogravimetric (TG) analysis as performed on a TG instrument (NETZSCH STA 409 PC) using a heating rate of 10 °C·min$^{-1}$ in air from 30 °C to 800 °C (CHN-O-Rapid). The X-ray photoelectron spectroscopy (XPS) analysis was performed on a Perkin eElmer PHI550 spectrometer with Al Ka (1486.6 eV) as the X-ray source. The $N_2$ adsorption/desorption tests are determined by Brunauer-Emmett-Teller (BET) measurements using an ASAP-2010 surface area analyzer. Electrical conductivity was measured by the conventional four-probe DC method (SDY-5 Four-Point probe meter).

### Electrochemical characterizations

Electrochemical evaluations were carried out by galvanostatic cycling with CR 2016-type coin cell. The working electrodes were formed by mixing 80 wt.% active materials, 10 wt.% carbon black, 10 wt.% polyvinylidene fluoride (PVDF) dissolved in N-methyl pyrrolidinone (NMP) and pasting the mixture on an

aluminum foil current collector. Afterwards, the electrode was dried under vacuum at 110 °C for 12 h. Test cells were assembled in an argon-filled glove box using Li foil as the counter electrode and polypropylene (PP) film as the separator. The electrolytes were 1 mol·L$^{-1}$ LiPF$_6$ solution in a 1:1 (V:V) mixture of ethylene carbon-ate (EC) and dimethyl carbonate (DMC). All the test cells assembly process was in an argon-filled glove box. In addition, The AC impedance spectrum was measured in the frequency ranges $10^{-2} \sim 10^5$ Hz. Galvanostatic charge-discharge cycling was conducted using a battery tester (LAND) with a voltage window of 1.0-3.0 V at different current rates of 0.5-30 C, where 1 C = 168.5 mAh g$^{-1}$.
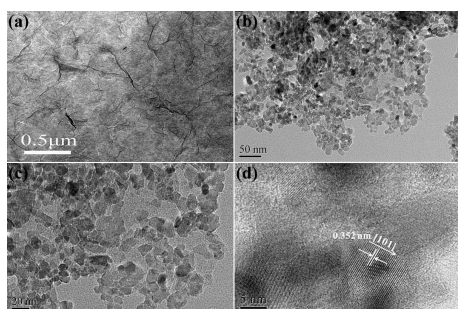
## Results and discussion



Fig. 1 TEM images of (a) GO, (b, c) H-TiO$_2$/RGO, and (d) HR-TEM image of H-TiO$_2$/RGO.

The morphologies and nanostructures of the pure GO obtained were investigated by TEM. Fig. 1a reveals that the two-dimensional graphene with wave-like structure is almost transparent nanosheets under the electron beam. They are not perfectly flat but display intrinsic microscopic roughening and out-of-plane deformations (wrinkles). As depicted in Fig. 1b and 1c, we can see that the TiO$_2$ nanopartical uniformly anchored on the surface of the graphene without serious aggregation. The corresponding HR-TEM image (Fig. 1d) shows clear lattice fringes, which allows for the identification of crystallographic spacing. The fringe spacing of *ca*. 0.352 nm matches that of the (101) crystallographic plane of anatase TiO$_2$.
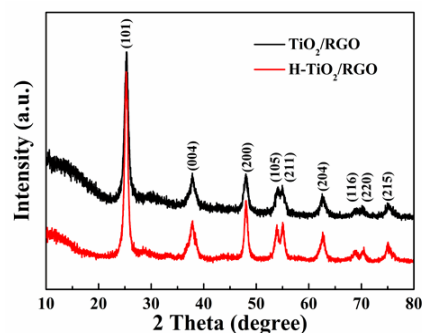


Fig. 2 XRD patterns of as-prepared TiO$_2$/RGO and H-TiO$_2$/RGO nanocomposite

As shown in figure 2, the prepared TiO$_2$/RGO and H-TiO$_2$/RGO nanocomposite were examined by powder XRD to determine the phase purities and grain sizes. The XRD pattern of the TiO$_2$/RGO nanocomposite exhibits typical peaks of anatase phase with a space group of I41/amd (JCPDS, No. 21-1272). And the prepared H-TiO$_2$/RGO nanocomposite shows nearly identical peak patterns as the pristine TiO$_2$/RGO material, indicating that no phase transition to rutile or other phases occurred. Moreover, it is noteworthy to mention that cccording to the broader and weaker diffraction peaks (200) of the synthesized TiO$_2$/RGO, indicating that the crystalline sizes of these materials are smaller than that of H-TiO$_2$/RGO nanocomposite. For the calcined samples, one can see that there is weak lattice expansion upon hydrogenation treatment, as would be expected because of lattice expansion upon reduction from Ti$^{4+}$ to Ti$^{3+}$. [34]
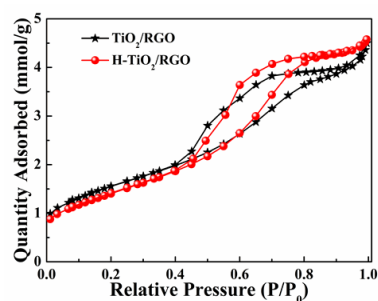


Fig. 3 Nitrogen adsorption-desorption isotherm curves of TiO$_2$/RGO and H-TiO$_2$/RGO

The Brunauer-Emmett-Teller (BET) specific surface area of the H-TiO$_2$/RGO and TiO$_2$/RGO were investigated by nitrogen isothermal adsorption. As shown in Fig. 3, which display a type IV isotherm with a well-defined hysteresis loop, indicating well-developed mesoporous characteristics. The specific surface areas of the TiO$_2$/RGO have been found to be 123.5 m$^2$ g$^{-1}$. While the H-TiO$_2$/RGO have lower specific surface areas of 114.4 m$^2$ g$^{-1}$, which may be caused by the weak lattice expansion of TiO$_2$
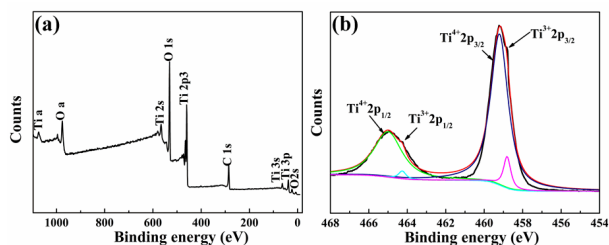
nanocrystallites through hydrogenation.



Fig. 5 (a) XPS survey spectra of H-TiO$_2$/RGO, and (b) typical high-resolution XPS of Ti2p for H-TiO$_2$/RGO.

To further confirm the elements and the chemical state of Ti ions in the H-TiO$_2$/RGO nanocomposite, the materials were investigated by the X-ray photoelectron spectroscopy (XPS). The XPS spectrum (Fig. 5a) indicated that the as-prepared H-TiO$_2$/RGO nanocomposite contained Ti, O, C. In Fig. 5b the doublet peaks at 458.3 and 464.1 eV corresponding to Ti2p$_{3/2}$ and Ti2p$_{1/2}$, demonstrating the existenceand occupying of Ti$^{4+}$ in an octahedral environment. Another pair of smaller peaks that can be found in 457.6 and 463.5 eV belongs toTi2p$_{3/2}$ and Ti2p$_{1/2}$, indicating the existence of Ti$^{3+}$,[36, 37] which suggesting the Ti$^{3+}$ sites were successful created in H-TiO$_2$/RGO nanocomposite during hydrogenation.
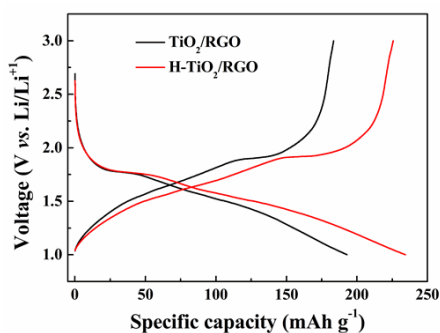


Fig. 6 Charge/discharge curves of TiO$_2$/RGO and H-TiO$_2$/RGO at a rate of 1 C.

Fig. 6 shows the representative discharge/charge voltage profiles of the electrodes made of TiO$_2$/RGO and H-TiO$_2$/RGO, at a current rate of 1 C within a cut off voltage window of 1.0-3.0 V, which are consistent with typical discharge/charge voltage profiles of TiO$_2$. It is evident that the discharge process of the three samples consists of three stages; the first stage is the quick voltage drop, the second stage is the distinct voltage plateau, and the third stage is a gradual decay in potential. The plateaus are related to the phase transition between the tetragonal and orthorhombic phases with Li insertion into anatase TiO$_2$.[38] Apparently, H-TiO$_2$/RGO can achieve a larger discharge capacity

of 234.4 mAh g$^{-1}$, while the TiO$_2$/RGO only exhibit a lower discharge capacity of 192.9 mAh g$^{-1}$. The obtained high lithium storage capacity of H-TiO$_2$/RGO can be attributed to the enhanced electric conductivity after the introduction of Ti$^{3+}$. Also, the voltage profiles of the TiO$_2$/RGO exhibited a relatively higher charging plateau and lower discharging plateau compared to the H-TiO$_2$/RGO hybrid, which is mainly related to the high electrode polarization.[39]
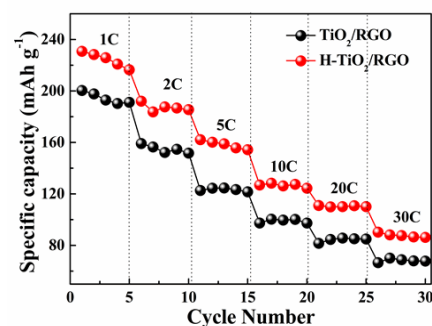


Fig. 7 Rate performance of TiO$_2$/RGO and H-TiO$_2$/RGO electrodes at different current rates.

The rate performances of TiO$_2$/RGO and H-TiO$_2$/RGO at the current rates of 1-30 C are compared in Fig. 7. Remarkably, as the discharge/charge rate increased from 1 C to 30 C, the discharge capacities of TiO$_2$/RGO decreased steeply, whereas the H-TiO$_2$/RGO nanocomposite decreased relatively slower at the same rate. By introducing Ti$^{3+}$ into TiO$_2$ nanocrystallites, which can substantially improve the electronic conductivity of TiO$_2$. Thus the H-TiO$_2$/RGO nanocomposite exhibited the highest rate capacity. It is noteworthy that the capacity (102.7 mAh g$^{-1}$) obtained by H-TiO$_2$/RGO nanocomposite at a rate of 30 C is higher than that obtained at a rate of 10 C for the TiO$_2$/RGO. It was reported that the good electronic conductivity and nanoparticles may contribute to the high rate discharge performance.[40] To confirm the improved electronic conductivity after introducing Ti$^{3+}$ into the TiO$_2$/RGO composite, we measured the electronic conductivity of the TiO$_2$/RGO and H-TiO$_2$/RGO nanocomposites. The H-TiO$_2$/RGO nanocomposites reveal a significant increase in electronic conductivity (ca. 0.1624 S·cm$^{-1}$) when compared with that of TiO$_2$/RGO composites (ca. 0.0016 S·cm$^{-1}$), demonstrating that after introducing Ti$^{3+}$ into TiO$_2$ nanocrystallites the improved electronic conductivity, promoting intrinsic electron and Li$^+$ transfer can result in a superior rate capability with high reversible capacity.
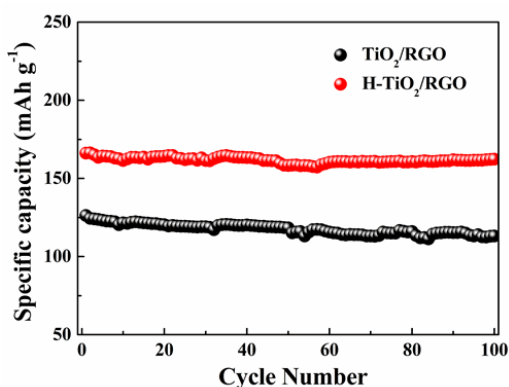
Fig. 8 Cycling performance of TiO$_2$/RGO and H-TiO$_2$/RGO between 1.0 and 3 V at 1 C rate.

The cycling behaviors for the three different samples at the rate of 5 C are shown in Fig. 8. The discharge capacity in the first cycle of the H-TiO$_2$/RGO nanocomposite was 166.3 mAh g$^{-1}$ at the rate of 5 C, after 100 cycles with only 2.4% capacity loss, but for TiO$_2$/RGO, the corresponding values were 129.3 mAh g$^{-1}$ and 12.5%, respectively. We compared this work with other TiO$_2$-based high-rate electrodes from recently literature[35, 42-45], and the results shown in Table 1. By comparison the capacitance value obtained at different current rates for our synthesized materials with those graphene-TiO$_2$-CNT nanocomposites [42], G-TiO$_2$ nanosheets [43], CNT@TiO$_2$-NSs [44], oxygen-deficient TiO$_{2-\delta}$ nanoparticles via hydrogen reduction[35] and CNTs–TiO$_{2-\delta}$ nanocomposites[45], the H-TiO$_2$/RGO hybrid nanostructures exhibits much better electrochemical properties than other TiO$_2$ based high rate electrode. This result demonstrates that the H-TiO$_2$/RGO nanocomposite is very stable, and the electrochemical Li$^+$ insertion/extraction process is quite reversible even at high rates. The high capacity, remarkable rate capability, and outstanding cycle stability of the H-TiO$_2$/RGO sheets may be caused by the synergistic coupling effects in the H-TiO$_2$ nanocrystals/RGO sheets (i) the H-TiO$_2$ nanocrystals not only greatly improved the electronic conductivity of TiO$_2$ but also drastically shorten the diffusion path for lithium-insertion/extraction as a result of the quantum size effect; (ii) the graphene sheets can act as a conductive substrate to improve the electron transport; (iii) the unique nanostructure not only provides a high surface area for improving the contact area between the electrode materials and electrolyte but also maintains the integrity of the electrode during the charge and discharge processes, which is responsible for the high rate capability and cycling stability.

Table 1. Comparison of rate capability (in mAh g$^{-1}$) at different current rates of H-TiO$_2$/RGO electrode with other TiO$_2$-based high-rate electrodes reported recently.

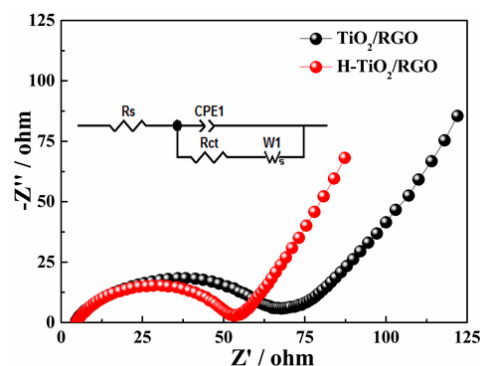| Samples | 1 C | 2 C | 5 C | 10 C | 20 C | 30 C |
|---|---|---|---|---|---|---|
| **H-TiO$_2$/RGO** | **230.8** | **192.1** | **162.2** | **128.4** | **111.1** | **90.3** |
| G-TiO$_2$-CNT | 163.7 | 150 | -- | 125 | -- | -- |
| G-TiO$_2$ NSs | 200 | -- | 125 | 119 | 107 | -- |
| CNT@TiO$_2$ | 194 | 175 | 148 | 115 | 75 | -- |
| TiO$_{2-\delta}$ Nps | 146 | 125 | 110 | 75 | 60 | 48 |
| CNTs–TiO$_{2-\delta}$ | 175 | -- | -- | 120 | -- | 50 |



Fig. 9 Electrochemical impedance spectra (EIS) of TiO$_2$/RGO and H-TiO$_2$/RGO electrodes. The inset shows the equivalent circuits used to fit the impedance spectra.

Table 2. Impedance parameters of the H-TiO$_2$/RGO and TiO$_2$/RGO electrodes.

| Sample | R$_s$ (Ω) | R$_{ct}$ (Ω) | CPE-T (μF) | i$^0$ (mA·cm$^{-2}$) |
|---|---|---|---|---|
| TiO$_2$/RGO | 4.3 | 64.13 | 82.59 | 0.40 |
| H-TiO$_2$/RGO | 3.6 | 48.75 | 65.86 | 0.53 |

To further testify the enhanced electronic conductivity, we carried out the EIS measurement for the H-TiO$_2$/RGO and TiO$_2$/RGO composites. Nyquist plots showed that both spectra consists of a depressed semicircle in high frequency region and an oblique straight line in low frequency region. The high frequency region of the semicircle attributes to the electrochemical reaction resistance and the double layer capacity of the electrode, while the low frequency region of the straight line corresponds to the diffusion of the lithium ions into the bulk of the anode material of the so-called Warburg diffusion.[43] The fitting results were obtained by ZView from Sai software set using an equivalent circuit. In this equivalent circuit, $R_s$ and $R_{ct}$ are the solution resistance and charge-transfer resistance, respectively. Constant phase-angle element (CPE) is placed to represent the double layer capacitance and passivation film capacitance. The exact kinetic differences between H-TiO$_2$/RGO and TiO$_2$/RGO composites were inspected by modeling AC impedance spectra based on the Randles equivalent circuit and

summarized in Table 1. It can be observed that the H-TiO$_2$/RGO electrodes exhibit much lower charge-transfer resistance than that of the TiO$_2$/RGO electrode. Furthermore, the exchange current density (i$^0$=RT/nFR$_{ct}$) of the H-TiO$_2$/RGO is higher than TiO$_2$/RGO. Therefore, the charge-transfer reaction of the H-TiO$_2$/RGO electrode takes place more than the TiO$_2$/RGO electrodes. Since the faradaic reaction is determined by ion transfer and electron conduction, the reduction of resistance might be attributed to the improved electronic conductivity of H-TiO$_2$/RGO electrodes induced by the introduction of Ti$^{3+}$ states. The highly conductive graphene sheets can facilitate electron transfer and thus decreasing resistance. Therefore, improved high discharge rate performance and the depressed polarization could be attributed to the substantial decrease in charge-transfer resistane.

## Conclusions

In summary, we have developed a facile one-pot route to synthesize H-TiO$_2$/RGO nanocomposites as advanced anode materials for high-rate LIBs. The H-TiO$_2$ nanoparticles were uniformly dispersed on the surface of RGO, which serve as the ideal host for fast and efficient lithium storage. The successfully introducing Ti$^{3+}$ states into TiO$_2$ nanocrystallites essentially improved the electronic conductivity of TiO$_2$, which is beneficial for the high-rate performance. This facile hydrogenation route to the fabrication of H-TiO$_2$-based nanocomposite can be expected to opens new perspectives to design high-performance electrode materials for lithium ion batteries.

## Acknowledgments

## Notes and references

College of Material Science and Engineering, Nanjing University of Aeronautics and Astronautics, Key Laboratory for Intelligent Nano Materials and Devices of Ministry of Education, Nanjing, 210016, P. R. China Fax: +86-025-52112626; Tel: +86-025-5211918;
E-mail: azhangxg@163.com

[1] B. Dunn, H. Kamath, J.M. Tarascon, *Science*, 2011, **334**, 928.

[2] M.M. Thackeray, C. Wolverton, E.D. Isaacs, Energy Environ. Sci., 2012, **5**, 7854.

[3] Z.G. Yang, J.L. Zhang, M.C.W. Kintner-Meyer, X.C. Lu, D. Choi, J.P. Lemmon, J. Liu, *Chem. Rev*., 2011, **111**, 3577.

[4] K.R. Stroukoff, A. Manthiram, *J. Mater. Chem*., 2011, **21**, 10165.

[5] F.T. Wagner, B. Lakshmanan, M.F. Mathias, *J Phys. Chem. Lett*., 2010, **1**, 2204.

[6] H. Buqa, D. Goers, M. Holzapfel, M.E. Spahr, P. Novak, *J. Electrochem. Soc*., 2005, **152**, A474.

[7] M. Winter, J.O. Besenhard, M.E. Spahr, P. Novak, *Adv. Mater*., 1998, **10**, 725.

[8] M. Wagemaker, A.P.M. Kentgens, F.M. Mulder, *Nature*, 2002, **418**, 397.

[9] A.R. Armstrong, G. Armstrong, J. Canales, P.G. Bruce, *Angew. Chem. Int. Ed*., 2004, **43**, 2286.

[10] A.R. Armstrong, G. Armstrong, J. Canales, R. Cracia, P.G. Bruce, *Adv.Mater*., 2005, **17**, 862.

[11] Z.H. Bi, M.P. Paranthaman, B.K. Guo, R.R. Unocic, C.A. Bridges, *J. Mater. Chem.* A, 2014, **2**, 1818.

[12] T.B. Lan, Y.B. Liu, J. Dou, Z.S. Hong, M.D. Wei, *J. Mater. Chem.* A, 2014, **2**, 1102.

[13] Y.S. Hu, L. Kienle, Y.G. Guo, J. Maier, *Adv. Mater*., 2006, **18**, 1421.

[14] Y.G. Guo, Y.S. Hu,W. Sigle, J. Maier, *Adv. Mater*., 2007, **19**, 2087.

[15] J.H. Liu, J.S. Chen, X.F. Wei, X.W. Lou, X.W. Liu, *Adv.Mater*., 2011, **23**, 998.

[16] M.M. Rahman, J.Z. Wang, M.F. Hassan, D. Wexler, H.K. Liu, *Adv. Energy Mater*., 2011, **1**, 212.

[17] L. Zhao, Y.S. Hu, H. Li, Z.X. Wang, L.Q. Chen, *Adv. Mater*., 2011, **23**, 1385.

[18] H. Han, T. Song, J.Y. Bae, L.F. Nazar, H. Kim, U. Paik, *Energy Environ.Sci*., 2011, **4**, 4532.

[19] Q.L. Wu, J. Li, R.D. Deshpande, N. Subramanian, S.E. Rankin, F. Yang, Y.T. Cheng, *J. Phys. Chem. C*, 2012, **116**, 18669.

[20] H. Han, T. Song, E.K. Lee, A. Devadoss, Y. Jeon, J. Ha, Y. C. Chung, Y.M. Choi, Y.G. Jung, U.Paik, *ACS Nano*., 2012, **6**, 8308.

[21] J.M. Szeifert, J.M. Feckl, D.F. Rohlfing, Y.Liu, V. Kalousek, J. Rathousky, T. Ben, *J. Am. Chem. Soc*., 2010, **132**, 12605.

[22] Y. Qiu, K. Yan, S.Yang, L. Jin, H. Deng, W. Li, *ACS Nano*., 2010, **4**, 6515.

[23] B. Wang, H.L. Xin, X.D. Li, J.L. Cheng, G.C. Yang, F.D. Nie, Scientific Reports, doi:10.1038/srep03729.

[24] H. Bai, Z. Liu, D. D. Sun, *J. Mater. Chem*., 2012, **10**, 1039.

[25] H.Q. Cao, B.J. Li, J.X. Zhang, F. Lian, X.H. Kong, M.Z. Qu, *J. Mater. Chem*., 2012, **22**, 9759.

[26] J.Y. Ma, D. Xiang, Z.Q. Li, Q. Li, X.K. Wang, L.W. Yin, CrystEngComm, 2013, **15**, 6800.

[27] S.M. Paek, E. Yoo, I. Honma, *Nano Lett*., 2009, **9**, 72.

[28] W. Li, F. Wang, S.S. Feng, J.X. Wang, Z.K. Sun, B. Li, D.Y. Zhao, *J. Am. Chem. Soc*., 2013, **135**, 18300.

[29] X. Lu, G. Wang, T. Zhai, M. Yu, J Gan, Y. Tong, Y. Li, *Nano Lett*., 2012, **12**, 1690.

[30] X. Chen, L. Liu, P. Y. Yu, S. S. Mao, *Science*, 2011, **331**, 746.

[31] A. Naldoni, M. Allieta, S. Santangelo, M. Marelli, F. Fabbri, S. Cappelli, C. L. Bianchi, R. Psaro and V. D. Santo, *J. Am. Chem. Soc.*, 2012, **134**, 7600.

5 [32] G. Wang, Y. Ling, Y. Li, *Nanoscale*, 2012, **4**, 6682.

[33] Y. Yan, B. Hao, D. Wang, G. Chen, E. Markweg, A. Albrecht, *J. Mater. Chem.* A, 2013, **1**, 14507.

[34] G.C. Li, Z.H. Zhang, H.R. Peng, K.Z. Chen, RSC Advances. 2013, **3**, 11507

10 [35] J.Y. Shin, J.H. Joo, D. Samuelis, J. Maier, *Chem. Mater.*, 2012, **24**, 543.

[36] W.S. Hummers, R.E. Offeman, *J. Am. Chem. Soc.*, 1958, **80**, 1339.

[37] Z.J. Yu, X.F Zhang, G.L. Yang, J. Liu, J.W. Wang, R.S. Wang, J.P. Zhang, *Electrochim. Acta*, 2011, **56**, 8611.

15 [38] J.Y, L. Qi, H.Y. Wang, *ACS Appl. Mater. Interf.*, 2011, **3**, 4315.

[39] J.S. Chen, Z.Y. Wang, X.C. Dong, P. Chen, X.W Lou, *Nanoscale*, 2011, **3**, 2158.

[40] L.F. Shen, C.Z. Yuan, H.J. Luo, X.G. Zhang, K. Xu, F. Zhang, *J. Mater. Chem.*, 2011, **21**, 761.

20 [41] B. Kang, G. Ceder, *Nature*, 2009, **458**, 190.

[42] L.F. Shen, X.G. Zhang, H.S. Li, C.Z. Yuan, G.Z. Cao, *J Phys. Chem. Lett.*, 2011, 2, 3096.

[43 S.J. Ding, J.S. Chen, D.Y. Luan, F.Y.C. Boey, S. Madhavi, X.W. Lou, *Chem. Commun.*, 2011, **47**, 5780.

25 [44] H.B. Wu, X.W. Lou, H.H. Hng, *Chem. Eur. J.*, 2012, **18**, 3132.

[45] E. Ventosa, P.R Chen, W. Schuhmann, W. Xia, *Electrochem. Commun.*, 2012, **25**, 132.

[46] K.M. Shaju, G.V. Subba Rao, B.V.R. Chowdari, *J. Electrochem.Soc.*, 2004, **151**, A1324.

**The table of contents entry**

Hydrogenated TiO$_2$/RGO nanocomposites have been synthesized *via* a facile one-pot hydrogenation, which exhibiting superior rate capability and outstanding capacity retention.